Characterization of Foam Flowing in a Granular Medium in Presence of Oil by Small Angle Neutron Scattering

Raphael Poryles, Thibaud Chevalier, Nicolas Gland, Elisabeth Rosenberg, Loïc Barré

Journal Name

ARTICLE TYPE

Cite this: DOI: 00.0000/xxxxxxxxxx

Characterization of Foam Flowing in a Granular Medium in Presence of Oil by Small Angle Neutron Scattering

Raphaël Poryles,*[a] Thibaud Chevalier,[a] Nicolas Gland,[a] Elisabeth Rosenberg[a] and Loïc Barré*[a]

Received Date
Accepted Date

DOI: 00.0000/xxxxxxxxxx

We present an experimental study of foam flow characterization inside a 3D granular medium packed in a cell. The foam is formed by coinjecting a surfactant solution and gas inside a cell filled with silica grains. The porous medium is initially saturated with dodecane and water before the gas-surfactant coinjection. To simplify the interpretation of the measurements, a contrast matching methodology has been applied in order to obtain a two phases system regarding the scattering length density values. The combination of transmission and incoherent scattering allow us to estimate the volume fractions of each phase whereas the coherent scattering is used to estimate the surface to volume ratio S/V related to water-oil and water-gas interfaces. Considering the evolution of S/V ratio, volume fractions and pressure difference, we infer some mechanisms of foam generation and transportation as well as oil removal.

1 Introduction

Foam injection in a porous medium is used in various industrial applications such as soil remediation[1,2] and oil extraction[3]. In oil industry, one challenge is to maximize the efficiency of the extraction. Typical oil fields production follows three stages. First a primary recovery simply relying on the natural pressure in the reservoir[4]. This is followed by a secondary recovery, by injection of a liquid to push the oil towards extraction wells. The residual oil saturation (S_{OR}) after this secondary stage is about 60 %[5] and the tertiary stage also called Enhanced Oil Recovery (EOR) implements various methods (chemical, thermical, gas injection) to increase the oil production and optimize the sweeping of the reservoir[4,6]. One of the methods considered is foam injection[7] as it decreases negative effects observed in the secondary oil recovery among which viscous fingering[8]. Understanding the dynamics of foam flowing in a porous medium is necessary to improve such technology.

Foam can be directly generated by coinjection of a gas and a surfactant solution in a porous medium[9]. The mechanisms of foam formation at the pore scale can be declined in three types: snap-off, leave behind and lamellae division[10]. When the foam is generated, an important increase of the pressure gradient is observed, resulting from the increase of effective gas viscosity and the decrease of relative permeability leading to a reduced mobility factor[8,11,12]. Many studies have been performed in quasi 2D Hele-Shaw cells and micromodels to observe the dynamics of the foam flow at the bubble scale[13–20]. Those experiments have shown many results including that bubbles can be trapped inside a single pore and that fragmentation and coalescence processes can occur. In 3D systems, the measurements are more complicated, since direct visualization is not possible. Some studies using computational tomography (CT scan) provided a good imaging of the foam generation in porous media, and a direct correlation between the pressure increase and the foam developping in the medium but the limited spatial resolution does not give access to the pore and lamellae scales[8,21–26].

One important issue for applications in oil industry is the effect of oil on the stability of the foam. In the presence of oil, the foam flow can be highly modified, and its relative viscosity decreased, leading to a decrease in efficiency[23,27–32].

In this work, we use neutron scattering to characterize the foam flowing in a 3D granular medium in presence of dodecane oil. The technique of neutron scattering is used in many soft matter systems to characterize complex materials, with a high resolution, down to around 10 Å[33,34]. Neutron scattering has been used to characterize bulk foam[35–38] and porous medium[39,40] but never, to our knowledge, in the case of a three phase flow (water/gas/oil) inside a porous matrix.

[a] IFP Energies nouvelles, 1 et 4 avenue de Bois-Préau, 92852 Rueil-Malmaison, France
* E-mail: raphael.poryles@yahoo.fr and loic.barre@ifpen.fr

By measuring neutron transmission and scattering and applying a phase contrast matching, we discuss the impact of oil on the foam formation inside the granular medium, and we access the different stages of oil transportation.

2 Experimental setup

2.1 Experimental setup

The experimental setup[41] is presented in Figure 1. The porous medium is contained in a silica cylindrical horizontal cell with a length l =7 cm and internal diameter d =4.2 mm. The cell is filled with hydrophilic silica grains, that were crushed and sieved at a size of 112-150 μm. By differential mass measurement of the cell, we measure a porosity of $\phi = 40$ %.

The outlet of the cell is connected to two 1 liter buffer bottles. Pressure in the buffer bottles is controlled using a back pressure regulator (Brooks, SLA5820B). This sets the pressure at the outlet of the cell. The produced fluids are collected after the back pressure regulator.

The different fluids coinjected at the inlet of the cell are the following: first an aqueous solution of SDS (Sodium Dodecyl Sulfate) at 2 g/L, and NaCl at 5 g/L. This solution is injected using a Vindum Pump (VP-12K). This concentration of SDS ensures that we are over the critical micellar concentration (CMC$\approx$ 1 g/L) and provides an important foamability, but is diluted enough to ensure a minimal number of micelles and consequently a low scattering contribution of the micelles in the scattering signal[42]. The second fluid is nitrogen gas (N_2), stored in a compressed bottle, and injected using a mass flow controller (Brooks, SLA5850S). A third injection is performed using a Pharmacia pump (P-500). This pump is used to inject the reference fluids and prepare the initial state. Those fluids are a 5 g/L NaCl water solution, and pure dodecane oil.

Pressure measurements are performed at the inlet and outlet of the cell, using absolute pressure sensors (Keller, PA-33X), from which we compute the differential pressure in the cell ΔP.

2.2 Experimental protocol

The goal of this experiment is to observe the influence of oil presence in the porous media. The cell is first completely saturated with the NaCl solution. Dodecane is then injected at a flow rate of 20 mL per hour during one hour. After this injection, the cell is in an irreducible water saturation state (S_{WI}). We then inject a NaCl solution at the same flow rate (20 mL per hour) for one hour in order to reach the residual oil saturation (S_{OR}). At this state, the oil is under the form of clusters or blobs dispersed in the pore network mainly saturated with brine.

To produce foam inside the porous medium, we directly coinject the SDS surfactant solution, and the nitrogen gas inside the cell at the S_{OR} state. The surfactant solution is injected at a flow rate of 4.5 mL/hr, and the gas is injected at a rate of 5.5mL/hr at 5 bars, which is the back pressure at the outlet of the cell. This gives a fractional gas flow rate of 55 %, also called foam quality[43].

The differential pressure ΔP is acquired every second of the experiment, which lasts for 14.5×10^4 s (about 40 hours).

During the experiment, neutron transmission and scattering are measured. The details on the neutron acquisition are presented in the following section.

2.3 SANS acquisition

The neutron line used is PA-20 of Orphée reactor at Laboratoire Léon Brillouin (LLB), Saclay (France).

The acquisitions are performed by measuring the neutron transmitted and scattered by the medium. A parallel neutron beam, 4 mm in diameter, crosses the cell at the middle of the granular medium. The neutron wavelength is selected at $\lambda = 4$ Å. The detector is placed at two different distances from the sample (2 m and 12 m), to capture two different range of wave vectors. At very small angles (12 m), the wave vector measured ranges from $q = 0.004$ to $q = 0.071$ Å^{-1} and at small angles (2 m) from $q = 0.022$ to $q = 0.449$ Å^{-1}. The two ranges overlap, so we can reconstruct the entire scattering spectrum between $q = 0.004$ and $q = 0.449$ Å^{-1}. The acquisition time is 15 minutes for each configuration. 2D isotropic raw intensities are converted to scattering differential section per unit volume $I(q)$ (cm^{-1}) following a standard procedure[33].

Additionally, we measure the transmission of the sample during two minutes with the detector at 12 m. The value of the transmission Tr is the total neutron flux measured crossing the cell φ_t during two minutes divided by the incident flux φ_i: $Tr = \varphi_t/\varphi_i$. This transmission corresponds to the neutrons not absorbed by the sample (scattered and non-scattered), and mainly depends on the quantity of oil and water in the cell.

To simplify the analysis, we used contrast matched solutions. The matching is performed using mixtures of deuterated and hydrogenated products[39,44]. We choose to match the scattering length density (SLD) of the water phases (NaCl solution and surfactant solution) to the granular medium, and the dodecane SLD to the N_2 gas one. Figure 2 gives the different scattering length densities of the products, calculated from atomic scattering lengths[45] and the corresponding matching. The water used to match the silica (SLD=3.475×10^{10} cm^{-2}) is a mixture of 40 % of H_2O and 60 % of D_2O in mass. The oil is matched with the N2 gas (SLD$\approx$ 0) with a mixture containing 89 % of $C_{12}H_{26}$ and 11 % of $C_{12}D_{26}$ in mass. Using this matching, we are able to obtain contrast between the silica + water phases and the gas + oil phases. This contrast matching of four different phases two by two is uncommon and remain sparse in the literature.

We first perform three references measurement: the dry granular medium, the water saturated medium, and the oil saturated medium. Transmission results are presented in Table 1. Figure 3 represents the scattering intensity measured $I(q)$ as a function of the wave vector q for the three references. The different references are for the medium in a dry [$\circ$], water saturated [$\diamond$] and oil saturated states [$\times$].

At small q values, a q^{-4} asymptotic behavior is observed and is related to the so called 'Porod' regime characteristic of smooth interfaces at q^{-1} length scales. At large q values, the scattered intensity is dominated by incoherent scattering that is proportional to the amount of hydrogen crossed by the beam. Some studies have shown that we can write the scattered intensity $I(q)$ for

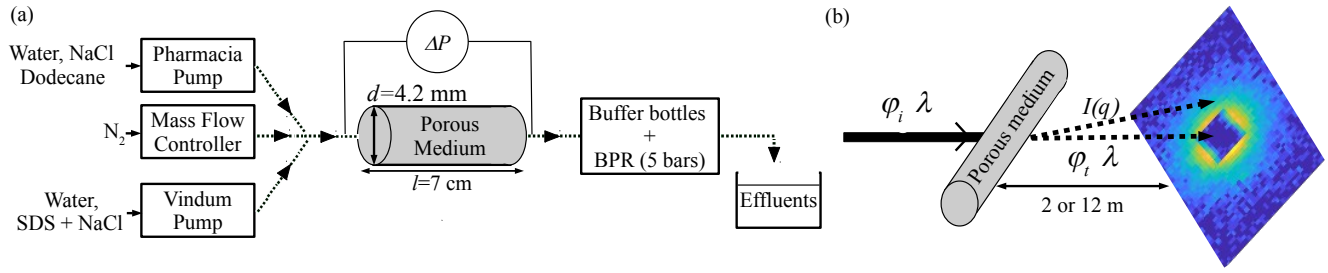

Fig. 1 (a) Experimental setup. The differential pressure ΔP is obtained from the pressure measured at the inlet and outlet of the cell. The reference NaCl solution and the dodecane is injected using a Pharmacia pump. The foam is created by coinjecting N_2 gas and a surfactant solution (SDS). A back pressure regulator sets the outlet pressure at 5 bar. (b) Schematic presentation of the neutron scattering line. The incident beam has a wavelength λ of 4 Å and a intensity I_i. The detector is placed at 2 or 12 m from the cell. The measured intensity on the detector is $I(q)$ and depends on the wave vector q.

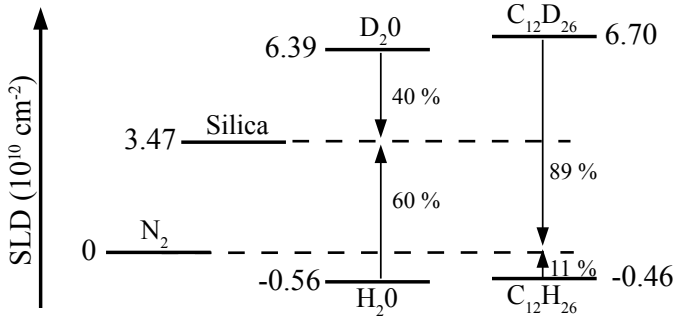

Fig. 2 Schematic view of the contrast matching. The water phase is matched with the silica (SLD=3.475×10^{10} cm^{-2}) and the oil phase is matched with the N_2 gas (SLD≈0). The percentage are expressed in mass.

foam[35,38] as:

$$I(q) = A/q^4 + B \quad (1)$$

The continuous line on Figure 3 shows the adjustment at low q: $I(q) \sim A.q^{-4}$ and at high q: $I(q) \sim B$.

By using a regression at low angles, we can define the ratio of the surface area over the total volume S/V[34] as:

$$S/V = A/(2\pi\Delta\text{SLD}^2) \quad (2)$$

where ΔSLD is the difference in the scattering length between the different phases (in our case, the grains/water, and the gas/oil). The values of the plateau B and the surface/volume ratio, for the different references are presented in Table 1.

We observe that the water and silica are correctly matched, since the coherent intensity scattered at low angles is very small (Figure 3 [◇], S/V in Table 1). For a similar reason, the oil and gas phases are also well matched, their intensity scattered at low angle is almost the same (Figure 3 [○, ×], S/V in Table 1). The observed differences gives a rough idea on error bars.

The value of the incoherent plateau B is given in Table 1. Since the incoherent scattering length of Si and O is null, the incoherent intensity is only related to hydrogen content (*i.e* oil and water). According to their composition, the various phases ranks as follows: $B_o > B_w > B_g$. In the following, the indexes w, o, g will correspond to the water, the oil and the gas phases respectively.

Figure 4 presents the intensity $I(q)$, in the cases of the initial state preparation: the irreducible water saturation state (S_{WI}, [○]) and the residual oil state (S_{OR}, [×]). The preparation of these states are presented in the previous section. The values of transmission Tr, ratio S/V, and incoherent plateau B are presented in Table 1. We observe that $B_{SWI} > B_{SOR}$ and $(S/V)_{SWI} > (S/V)_{SOR}$, which is coherent with the fact that the S_{WI} state contains more oil than the S_{OR} state. Note that the grains are hydrophilic and are always covered with water (there is no oil-grains interfaces, except for the reference oil sample).

To estimate the saturation of the water phase Φ_w and the oil phase Φ_o, we write the value of the measured plateau B as:

$$B = B_w.\Phi_w + B_o.\Phi_o \quad (3)$$

where $B_{w,o}$ is the value for the references.

By having $\Phi_w + \Phi_o = 1$, and solving the system, we have $\Phi_w^{SWI} = 0.45$, $\Phi_w^{SOR} = 0.82$, so $\Phi_o^{SWI} = 0.55$, $\Phi_o^{SOR} = 0.18$.

Once we reach the S_{OR} state, the coinjection of gas and surfactant solution is started, to generate the foam inside the porous medium.

Table 1 Reference values for the transmission Tr, the ratio S/V, and the incoherent plateau B

	Dry	Water	Oil	S_{WI}	S_{OR}
Tr	0.87	0.58	0.39	0.45	0.57
$S/V(cm^{-1})$	619	5	636	267	149
$B(cm^{-1})$	0.001	0.020	0.065	0.045	0.028

3 Observations and analysis

3.1 Pressure evolution

The continuous line in Figure 5 shows the evolution of the differential pressure ΔP with time t. During a first phase (stage I), the differential pressure is small (≈ 50 mbar) and does not change until $t \approx 6 \times 10^4$ s. During this phase, foam is not yet formed, at the

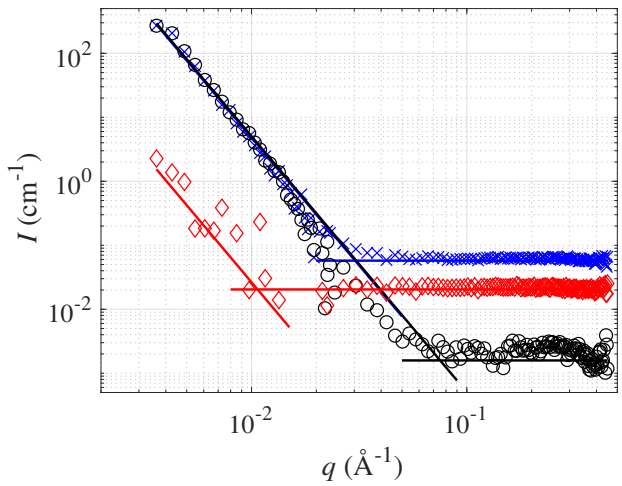

Fig. 3 Intensity $I(q)$ as a function of the wave vector q for the three references. [○: Dry medium], [×: Oil saturated], [◇: Water saturated]. The solid lines represent the adjustment in $I \sim q^{-4}$ and $I = B$.

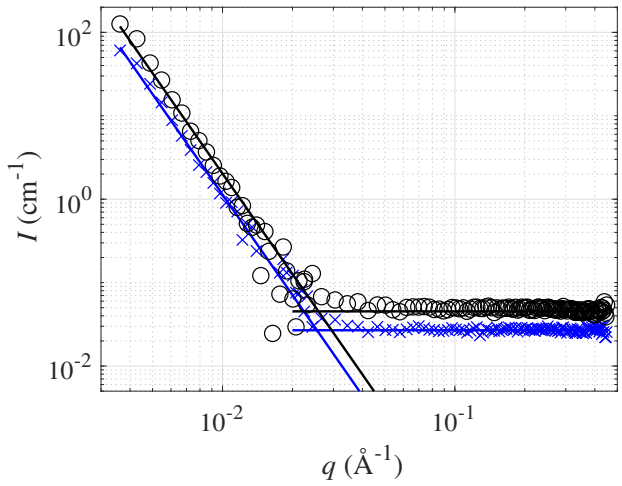

Fig. 4 Reference for the initial S_{WI} state [○] and the S_{OR} state[×]. The solid lines represent the adjustment in $I \sim q^{-4}$ and $I = cst$.

outlet of the cell we only observe a succession of liquid and gas phase. The pressure slowly increases until $t \approx 9 \times 10^4$ s (stage II), and then rapidly increases up to a pressure $\Delta P = 3.5$ bars during stage III. At this point, we observe a well formed foam at the outlet of the cell. A second jump is observed, and the differential pressure finally stabilizes at $\Delta P \approx 4.5$ bars (stage IV). Preliminary tests (without neutron scattering) only showed one jump, with the same final value ($\Delta P \approx 4.5$ bars). Therefore the second jump remains to be explained.

The ○ symbols represent the times when neutron scattering has been measured. Since each acquisition lasts for 45 minutes, the points are represented at the half time of each measurement.

The three colored dots correspond to three examples shown in the following subsection.

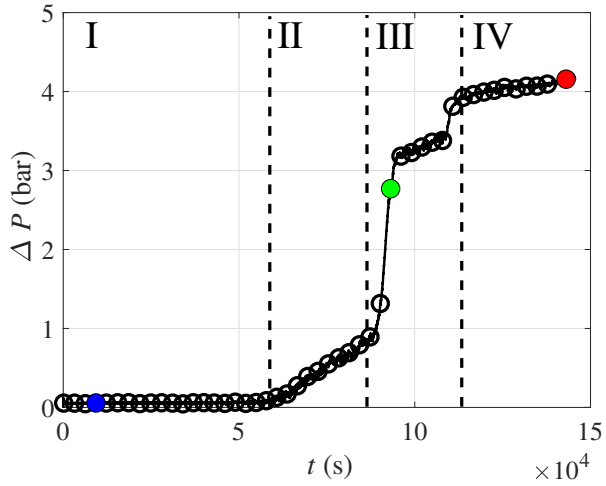

Fig. 5 differential pressure ΔP as a function of time t. The circles represent the times when neutron scattering are measured. The three colored points correspond to the examples given in Figure 6.

3.2 Scattering spectrum

During the gas injection, we acquired data at two different configurations. First we acquired during two minutes the transmission Tr with the detector placed at 12 m of the sample. After this first acquisition, we measure the neutron scattering of the sample (low q), with the detector at 12 m. The detector is then positioned at 2 m from the sample and scattering is again measured (high q). Finally, the detector is brought back to 12 m and the measurement cycle starts again. This process lasts for about 45 minutes, which includes the time to change the detector positions. Each configuration has been presented in Section 2.2.

Figure 6 shows three examples of neutron scattering spectrum $I(q)$ corresponding to the colored dots on Figure 5: [×] at the beginning of injection when no foam is formed, [○] at the pressure jump when foam starts to be created, [◇] when the the stationary regime is reached. The solid lines represent the adjustment in $I(q) \sim q^{-4}$ and $I(q) = cst$ (Equation 1). We measure the incoherent plateau B as well as the prefactor at low wave vectors A which gives us access to ratio S/V (Equation 2).

We see that for those particular cases, the prefactor A increases with time (so does the ratio S/V), while the level of the plateau B decreases. This will be discussed in detail in the following sections.

4 Results

4.1 Transmission

The Figure 7 represents the evolution of transmission Tr versus time t. The three colored dots correspond to the examples in Figure 6. We observe that the transmission follows the pressure curve (Figure 5). At the beginning of injection, the transmission is small, due to an important quantity of oil and water in the system. Once the foam is generated, the transmission increases rapidly, until it reaches a final state at $Tr \approx 0.80$.

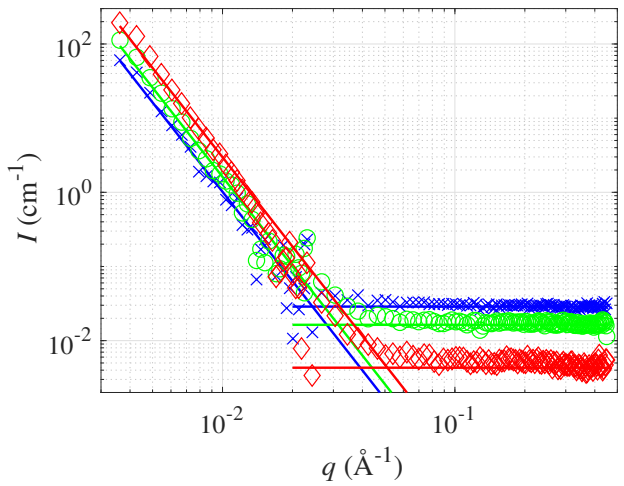

Fig. 6 Intensity $I(q)$ as a function of the wave vector q for three examples during the experiment. [×: beginning of injection] [○: at the transition] [◇: in the stationary regime]. The solid lines represent the adjustment in $I \sim q^{-4}$ and $I = cst$.

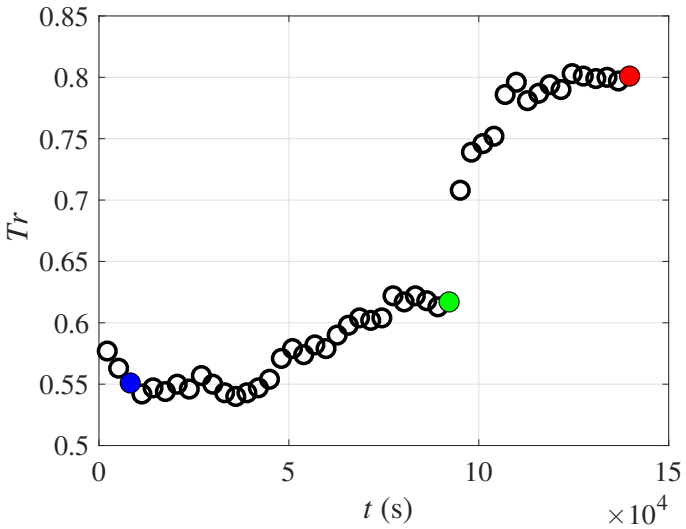

Fig. 7 Transmission coefficient Tr as a function of time t. The three colored points correspond to the examples given in Figure 6.

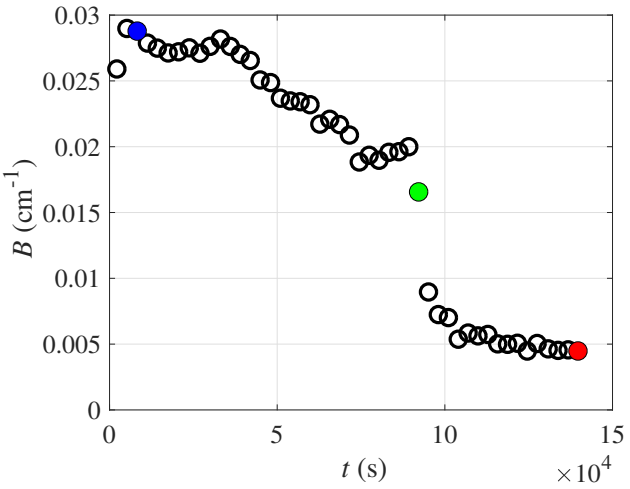

Fig. 8 Value of the incoherent plateau B (see Equation 1) as a function of time t. The three colored points correspond to the examples given in Figure 6.

4.2 Incoherent plateau

At large q, the scattering intensity $I(q)$ is constant (B in Equation 1). Using a linear regression, we can access the value of this incoherent plateau for each acquisition (with the detector at 2 m). Figure 8 shows the value of this incoherent plateau as a function of time. The colored dots represent the examples given in Figure 6. We see that the evolution of the plateau is in opposition with the pressure change. At the start of the experiment $B \approx 0.027$, and its value decreases slowly towards $B \approx 0.02$ until foam starts forming, when its value drops to 0.005.

4.3 Phase saturation

Using the previous results on the transmission value Tr and the incoherent plateau B, we get access to the saturation of each phase inside the porous matrix. We first write that the sum of the three phases volume fraction is equal to 1:

$$\Phi_w + \Phi_g + \Phi_o = 1 \tag{4}$$

where Φ_w, Φ_g and Φ_o are the volume fraction of water, gas and oil phase in the porous volume.

Using the transmission measurement, we deduce the μ coefficient given by Beer-Lambert law as:

$$\mu_{w,o} = -ln(\frac{Tr_{w,o}}{Tr_{dry}})/(d.\phi) \tag{5}$$

where $Tr_{w,o}$ is the transmission of the water and oil references respectively, Tr_{dry} the dry reference, d the internal diameter of the cell, and ϕ the porosity.

The value of the incoherent plateau B is given at each time by equation 3 in Section 2.3:

$$B = B_w.\Phi_w + B_o.\Phi_o$$

with $B_{w,o}$ the incoherent plateau for the references and $\Phi_{w,o}$ the percentage of water and oil phases in the porous volume (we assume that the incoherent plateau for the gas phase is negligible).

In the same way, we can write down for the transmission measured

$$-ln(Tr/Tr_{dry})/d.\phi = \mu_w.\Phi_w + \mu_o.\Phi_o \tag{6}$$

Writing down $\alpha = -ln(Tr/Tr_{dry})/(d.\phi)$, and combining Equations 3 and 6, we can finally write for the three phases:

$$\Phi_o = (\alpha - (\mu_w.B/B_w))/(\mu_o - (\mu_w.B_o/B_w)) \tag{7}$$

$$\Phi_w = (\alpha - (\mu_o.B/B_o))/(\mu_w - (\mu_o.B_w/B_o)) \tag{8}$$

$$\Phi_g = 1 - \Phi_w - \Phi_o \tag{9}$$

The Figure 9 presents the three phases volume fraction [◇, Φ_w]

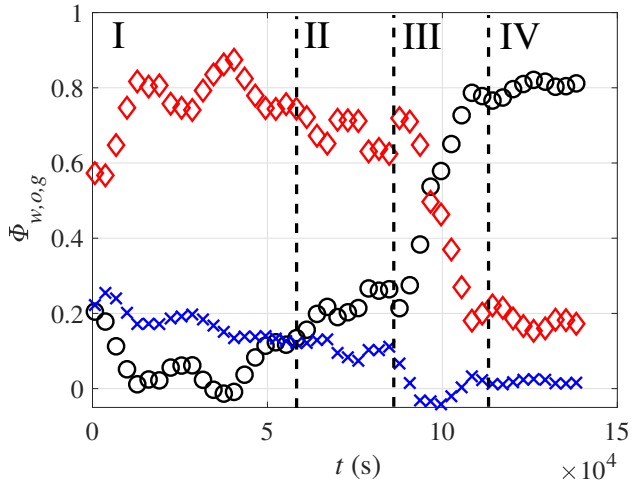

Fig. 9 Phase proportions $\Phi_{w,o,g}$, as a function of time. [$\diamond$: Water phase Φ_w] [$\times$: Oil phase Φ_o] [$\circ$: Gas phase Φ_g]. The four stage of foam formation (I-IV) will be presented in Section 5.

, [$\times$, Φ_o] and [$\circ$, Φ_g] as a function of time t. Considering that we have three coupled equations, the solution presents strong fluctuations due to the computation and to the uncertainty of our measurements. We recall that B and Tr are acquired sequentially. Therefore, the error on fluids saturation is particularly important when these quantities vary strongly. This is illustrated during stage III when non physical (negative) values for Φ_o are computed. During stage I, Φ_o slightly decreases. In stage II, Φ_g starts to increase due to the start of foam formation correlated to the increase of differential pressure ΔP in Figure 5. Then Φ_g jumps up to 80% and Φ_w drops (stage III). In stage IV the three different phases saturations remain roughly constant.

4.4 Ratio S/V

By measuring the prefactor A at low angles scattering, we can get the ratio S/V (see Section 2.3). S/V is related to the scattering interfaces, oil/water and gas/water:

$$\left(\frac{S}{V}\right) = \left(\frac{S}{V}\right)_{o-w} + \left(\frac{S}{V}\right)_{g-w}$$

For each contribution, S/V is related to the phase concentration and the size of the scattering objects. For monodisperse and spherical objects of radius R_p and volume fraction ϕ, one can write:

$$\left(\frac{S}{V}\right) = \left(\frac{3\phi}{R_p}\right) \tag{10}$$

R_p is also called the Porod radius[34]. In our case, for instance in the water-oil interface, we have $R_p^{o-w} = (3.\phi.\Phi_o)/(S/V)_{o-w}$.

The evolution of this ratio with time is presented in Figure 10. Once again we find that this prefactor is correlated with the pressure variation, and thus the foam formation. This is an important result since it shows that the texture of the foam is continuously changing as the pressure gradient is increased. This ratio slightly decreases from 150 down to 100 cm^{-1} (stage I), then it increases back during stage II. In stage III it rises sharply up to 570 cm^{-1}. Finally it slowly reduces down to 400 cm^{-1} (stage IV).

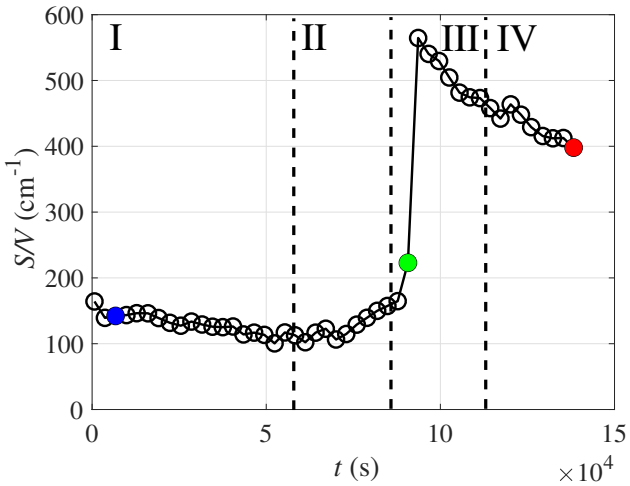

Fig. 10 Ratio S/V (see Equation 1) as a function of time t. The three colored points correspond to the examples given in Figure 6. The four stages of foam formation (I-IV) will be discussed in detail Section 5.

5 Discussion

In this section we propose an interpretation of the four different stages (I-IV) identified on Figures 5,9 and 10.

During stage I, the differential pressure ΔP remains close to zero and no foam is formed. The gas follows preferential paths through the matrix which is confirmed by a low Φ_g. The main contribution of the ratio S/V comes from the oil-water interface. Moreover this ratio S/V decreases slowly, as does the oil content Φ_o. Computing the equivalent Porod radius for the oil phase, we obtain at the beginning of this first stage $R_p^{o-w} \approx 16.0$ μm and at the end $R_p^{o-w} \approx 15.6$ μm. This shows that the oil blobs are removed, without evolution of their average radius, from $\Phi_o \approx 0.23$ to $\Phi_o \approx 0.13$. With the same method, one can determine a characteristical length of the porous medium from the dry state $R_p^{dry} \approx 19.0$ μm (S/V in Table 1), intermediate between the pore and throat sizes. This would be in agreement with the oil blobs being localized inside the pores. In practice during this stage, the oil blob removal is induced by the presence of the surfactant which decreases the interfacial tension.

In stage II, a small increase of differential pressure ΔP, gas fraction Φ_g and ratio S/V is observed. This shows the beginning of partial foam formation inside the porous medium. Since the oil follows the same trend as in stage I, we believe that the foam is created in the oil depleted zones, and the oil is still removed by surfactant action.

The beginning of stage III presents a sharp increase of differential pressure ΔP, gas fraction Φ_g and ratio S/V as well as a sharp decrease of Φ_w. The foam has then invaded most of the porous medium and is fully structured with a fine texture (im-

portant S/V and ΔP). Most of the remaining oil has been flushed outside of the porous medium by the foam invasion. Finally in stage IV the differential pressure and the phases concentration show an asymptotic behavior and tend to a constant value: the foam is in its completely structured form.

One interesting issue is the significant decrease of S/V in the stage III and IV. Since the pressure increases during this time, foam contribution can only lead to an increase of S/V ratio. Thus the oil-water interface evolution is the only possible reason for such evolution. This decrease being important ($\sim 30\%$ of the maximum), and the oil being in small quantity (estimated as less than 2% of the volume), this remaining oil can only be present in the form of small droplets removed during this final stage. The S/V ratio tends to a asymptotic final value where we suppose that all the oil is removed ($\Phi_o = 0$). From the S/V ratio decrease, from 564 to 398 cm^{-1}, one can estimate the maximum radius of the removed oil droplets as $R_p^{o-w} < 1.4\ \mu$m. This is at least one order of magnitude smaller than the initial oil blob size in stage I. We believe that this droplet transport is performed inside the foam plateau borders, nodes and the lamellae. These mechanisms have been reported in the literature[46,47].

6 Conclusion

We present a new approach based on small angle neutron scattering to study foam transport in a representative 3D porous medium, in the presence of oil. This work is innovative in the technique used where four phases contrast matching has been performed: the SLD of water is matched to the silica grains one and the oil to the gas. It gives us access to a better spatial resolution compared to the usual measurements (CT-Scan and micro-models). By combining the transmission and the incoherent plateau, we estimated the three phases saturations in the porous volume. The strong added value is the measurement of the ratio S/V which gives us an information on the size of the scattering objects over a few order of magnitude. From this characterization we can infer the mechanisms of foam generation and transportation as well as oil removal. At the beginning of the coinjection, oil blobs are removed by the surfactant without significative variation of their size. The foam is first generated in the most permeable paths and area already swept by the surfactant. The foam then structures itself and invades the entire medium, flushing the residual oil. An interesting result is that, in the final stage, the oil transported by the foam is in a form of small droplets.

We believe that these results could open a more general usage of neutron scattering for the study of foam flow especially in porous media, and this work shows the potentiality of it. The most striking contribution of such approach is to discriminate among the different mechanisms proposed in the literature for oil transportation by foam in a 3D representative porous medium. As a future work, to fully exploit neutron capabilities, one could explore more in details the scattering spectrum at intermediate wave vectors. This could give access to other information such as the shape, size and concentration of lamellae, oil droplets and micelles. Another study axis would be to vary the injection conditions such as the flow rates, the surfactant nature or the salinity.

Acknowledgements

The neutron measurements have been performed on the PA-20 line at LLB Laboratory, CEA Saclay (France) under the project 910. We particularly thank for his help our local contact J. Jestin. The participants on the shifts were L. Barré, T. Chevalier, A. Fafet, N. Gland, P. Hayrault, F. Lutz, N. Pannacci, R. Poryles and E. Rosenberg (alphabetical order).

Notes and references

1 K. R. Reddy, S. Kosgi and J. Zhou, *Hazard. Waste Hazard.*, 1995, **12**, 97–118.
2 K. R. Reddy, R. Semer and J. A. Adams, *Environ. Manage. Health*, 1999, **10**, 52–63.
3 H. Hemaptur, S. M. Mahmood, N. H. Nasr and K. A. Elraies, *J. Nat. Gas Sci. Eng.*, 2018, **53**, 163–180.
4 S. Thomas, *Oil Gas Sci. Technol.*, 2008, **63**, 9–19.
5 A. Muggeridge, A. Cockin, K. Webb, H. Frampton, I. Collins, T. Moulds and P. Salino, *Phil. Trans. R. Soc. A*, 2014, **372**, 201220320.
6 M. F. Nazar, S. S. Shah and M. A. Khosa, *Pet. Sci. Technol.*, 2011, **29**, 1353–1365.
7 R. Farajzadeh, A. Andrianov, R. Krastev, G. J. Hirasaki and W. R. Rossen, *Adv. Colloid. Interfac.*, 2012, **183**, 1–13.
8 M. Simjoo, Q. P. Nguyen and P. L. J. Zitha, *Ind. Eng. Chem. Res.*, 2012, **51**, 10225–10231.
9 A. Turta and A. Singhal, *J. Can. Petrol. Technol.*, 2002, **41**, 1–43.
10 T. C. Ransohoff and C. J. Radke, *SPE Reservoir Eng.*, 1988, **3**, 573–585.
11 A. H. Falls, J. J. Musters and J. Ratulowski, *SPE Reservoir Eng.*, 1989, **4**, 155–164.
12 H. O. Lee, J. P. Heller and A. Hoefer, *SPE Reservoir Eng.*, 1991, **6**, 421–428.
13 A. A. Kellerm, M. J. Blunt and P. V. Roberts, *Transport Porous Med.*, 1997, **26**, 277–297.
14 I. BenSalem, I. Cantat and B. Dollet, *Colloid. Surface A*, 2013, **438**, 41–46.
15 B. Geraud, S. A. Jones, I. Cantat, B. Dollet and Y. Méheust, *Water Resour. Res.*, 2016, **52**, 773–790.
16 C. Micheau, E. Rosenberg, L. Barré and N. Pannacci, *Colloid. Surface A*, 2016, **501**, 122–131.
17 B. Geraud, Y. Méheust, I. Cantat and B. Dollet, *Phys. Rev. Lett.*, 2017, **118**, 098003.
18 S. A. Jones, N. Getrow and S. Vincent-Bonnieu, *Soft Matter*, 2018, **14**, 3490–3496.
19 S. A. Jones, N. Getrow and S. Vincent-Bonnieu, *Soft Matter*, 2018, **14**, 3497–3503.
20 C. Yeates, S. Youssef and E. Lorenceau, *Colloid. Surface A*, 2019, **575**, 184–198.
21 S. Akin and A. R. Kovscek, *Geol. Soc. Spec. Publ.*, 2003, **215**, 23.

22 Q. P. Nguyen, P. K. Currie, M. Buijse and P. L. J. Zitha, *J. Petrol. Sci. Eng.*, 2007, **58**, 119–132.
23 A. Andrianov, R. Farajzadeh, M. M. Nick, M. Talanana and P. L. J. Zitha, *Ind. Eng. Chem. Res.*, 2012, **51**, 2214–2226.
24 A. Haugen, N. Mani, S. Svenningsen, B. Brattekås, A. Graue, G. Ersland and M. A. Fernø, *Transport Porous Med.*, 2014, **104**, 109–131.
25 M. Simjoo and P. L. J. Zitha, *Transport Porous Med.*, 2015, **107**, 799–820.
26 C. Ouali, E. Rosenberg, L. Barré and B. Bourbiaux, *Oil Gas Sci. Technol.*, 2019, **74**, 13.
27 T. Lu, Z. Li, S. Li, S. Liu, X. Li, P. Wang and Z. Wang, *Transport Porous Med.*, 2015, **109**, 25–42.
28 M. M. Almajid and A. R. Kovscek, *Adv. Colloid. Interfac.*, 2016, **233**, 65–82.
29 G. Batôt, M. Fleury, E. Rosenberg, L. Nabzar and M. Chabert, *SPE EOR Conf.*, 2016, 179855.
30 K. Osei-Bonsu, P. Grassia and N. Shokri, *Fuel*, 2017, **203**, 403–410.
31 M. Amirmoshiri, Y. Zeng, Z. Chen, P. M. Singer, M. C. Puerto, G. Grier, R. Z. K. Bahrim, S. Vincent-Bonnieu, R. Farajzadeh, S. L. Biswal and G. J. Hirasaki, *Energ. Fuel*, 2018, **32**, 11177–11189.
32 J. Tang, S. Vincent-Bonnieu and W. R. Rossen, *Energy*, 2019, **188**, 116022.
33 I. Grillo, *Small-Angle Neutron Scattering and Applications in Soft Condensed Matter*, Springer, 2008.
34 F. Cousin, *EPJ Web Conf.*, 2015, **104**, 01004.
35 M. A. V. Axelos and F. Boué, *Langmuir*, 2003, **19**, 6598–6604.
36 J. Etrillard, M. A. V. Axelos, I. Cantat, F. Artzner, A. Renault, T. Weiss, R. Delannay and F. Boué, *Langmuir*, 2005, **21**, 2229–2234.
37 C. Micheau, P. Bauduin, O. Diat and S. Faure, *Langmuir*, 2013, **29**, 8472–8481.
38 A. Mikhailovskaya, L. Zhang, F. Cousin, F. Boué, P. Yazhgur, F. Muller, C. Gay and A. Salonen, *Adv. Colloid Interfac.*, 2017, **247**, 444–453.
39 Z. Mileeva, D. K. Ross, D. Wilkinson, S. M. King, T. A. Ryan and H. Sharrock, *Carbon*, 2012, **50**, 5062–5075.
40 C. J. Jafta, A. Petzold, S. Risse, D. Clemens, D. Wallacher, G. Goerigk and M. Ballauf, *Carbon*, 2017, **123**, 440–447.
41 C. Ouali, *Caraterisation multi-echelle de l'ecoulement de mousses en milieux poreux en contexte EOR*, PhD Thesis, 2019.
42 B. Cabane, R. Duplessix and T. Zemb, *J. Physique*, 1985, **46**, 2161–2178.
43 R. Farajzadeh, M. Lottfollahi, A. A. Eftekhari, W. R. Rossen and G. J. H. Hirakasi, *Energ. Fuel*, 2015, **29**, 3011–3018.
44 M. Adamo, A. S. Poulos, R. M. Miller, C. G. Lopez, A. Martel, L. Porcar and J. T. Cabral, *Lab Chip*, 2017, **17**, 1559–1569.
45 L. A. Feigin and D. I. Svergun, *Structure Analysis by Small-Angle X-Ray and Neutron Scattering*, Plenum Press, New York and London, 1987.
46 V. Bergeron, M. E. Fagan and C. J. Radke, *Langmuir*, 1993, **9**, 1704–1713.
47 D. J. Manlowe and C. J. Radke, *SPE*, 1990, 18069.